The Journal of Experimental Biology 215, 2072-2080

doi:10.1242/jeb.058172

Localized fluidization burrowing mechanics of *Ensis directus*

Amos G. Winter, V*, Robin L. H. Deits and A. E. Hosoi

Department of Mechanical Engineering, Massachusetts Institute of Technology, 77 Massachusetts Avenue, Cambridge, MA 02139, USA

*Author for correspondence (awinter@mit.edu)

SUMMARY

Muscle measurements of *Ensis directus*, the Atlantic razor clam, indicate that the organism only has sufficient strength to burrow a few centimeters into the soil, yet razor clams burrow to over 70 cm. In this paper, we show that the animal uses the motions of its valves to locally fluidize the surrounding soil and reduce burrowing drag. Substrate deformations were measured using particle image velocimetry (PIV) in a novel visualization system that enabled us to see through the soil and watch *E. directus* burrow *in situ*. PIV data, supported by soil and fluid mechanics theory, show that contraction of the valves of *E. directus* locally fluidizes the surrounding soil. Particle and fluid mixtures can be modeled as a Newtonian fluid with an effective viscosity based on the local void fraction. Using these models, we demonstrate that *E. directus* is strong enough to reach full burrow depth in fluidized soil, but not in static soil. Furthermore, we show that the method of localized fluidization reduces the amount of energy required to reach burrow depth by an order of magnitude compared with penetrating static soil, and leads to a burrowing energy that scales linearly with depth rather than with depth squared.

Key words: burrowing, bivalve, fluidization, particle image velocimetry, soil mechanics.

Received 28 March 2011; Accepted 29 February 2012

INTRODUCTION

There are many examples of animals that live in particulate substrates and have adapted unique locomotion schemes. The sandfish lizard (*Scincus scincus*) wiggles its body from side to side in order to effectively swim through sand (Maladen et al., 2009). Smaller organisms, such as nematodes (*Caenorhabditis elegans*), have been observed to move quite efficiently *via* an undulatory motion in saturated granular media (Jung, 2010a; Wallace, 1968). Clam worms (*Nereis virens*) have been observed to burrow in gelatin, a material with properties similar to those of elastic muds, by propagating a crack (Dorgan et al., 2005). Throughout this paper, we use the terms 'soil' and 'substrate' to refer to the media in which burrowing organisms live, regardless of whether they are granular or cohesive. We specify that these substrates are composed of small particles (from clay to coarse sand) with the term 'particulate'.

Numerous soft-bodied organisms that live in particulate substrates saturated with a pore fluid use a two-anchor system to burrow: one section of the animal expands to form an anchor while another section contracts and extends to progress forward in the burrow; once extension is exhausted, the roles of each section are reversed (Dorgan et al., 2005; Fager, 1964; Holland and Dean, 1977; Jung, 2010b; Shin et al., 2002; Stanley, 1969; Trueman, 1966a; Trueman, 1966b; Trueman, 1967; Trueman, 1975). In this paper, we show that the Atlantic razor clam (*Ensis directus* Conrad 1843), which burrows *via* the two-anchor method, uses motions of its valves to create a pocket of fluidized substrate around its body to reduce drag forces and burrowing energy expenditure.

Trueman measured ~10 N as the maximum pulling force that *E. directus* can exert to pull its valves into soil (Trueman, 1967). Using a blunt body with a size and shape similar to that of *E. directus*, pressed into the animal's habitat soil on a mud flat in Gloucester, MA, we measured that 10 N of force should enable *E. directus* to submerge to approximately 1–2 cm. In reality, razor clams can dig to 70 cm (Holland and Dean, 1977). Because drag force scales linearly with depth for a body moving through a granular medium (Robertson and Campanella, 1983), muscle force measurements indicate that *E. directus* is approximately 75 times too weak to reach full burrow depth in static soil. Thus, the animal must manipulate the surrounding environment to reduce drag.

Ensis directus is enclosed by two, long, slender valves that hinge along an axis oriented longitudinally to the animal. A foot, which is a dexterous, soft organ, resides at the bottom of the valves. *Ensis directus* burrows by using a series of valve and foot motions to draw itself into the substrate (Fig. 1). We estimate an upper bound of the mechanical energy per depth for the animal to advance its valves downwards by adapting pedal strength, valve displacement, hinge stiffness and mantle cavity pressure measurements from Trueman (Trueman, 1967) and summing the expended mechanical energy and attained displacements for each burrowing motion: valve uplift (0.05 J, 0.5 cm), valve contraction (0.07 J, 20 deg) and valve penetration (0.20 J, –2.0 cm), for a total of 0.21 J cm^{-1}. Re-expansion of the valves is accomplished through elastic rebound of the hinge ligament and thus requires no additional energy input by the animal. To put the magnitude of the energetics in perspective, *E. directus* can travel over 0.5 km through soil on the energy stored in a AA battery (Energizer, 2009).

MATERIALS AND METHODS

Specimen collection

Ensis directus specimens used for our research were collected from natural stocks in Orleans and Gloucester, MA, under the appropriate research permits issued by the Massachusetts Department of Fish and Game. Once specimens were harvested and brought back to the laboratory, they were held in a chilled, saltwater commercial lobster tank (50-gallon lobster tank, Stark Products, College Point, NY, USA).

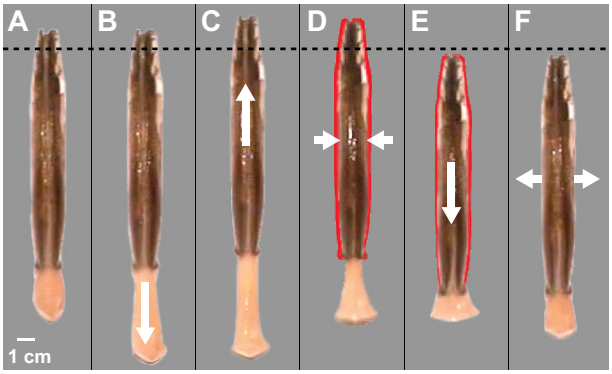

Fig. 1. *Ensis directus* burrowing motions. The dashed line indicates the depth datum. White arrows denote valve and foot motions. Panels are snapshots of live *E. directus* performing burrowing motions. The red silhouette denotes valve geometry in the expanded state, before contraction. (A) Start of burrowing cycle. (B) Foot extends downward. (C) *E. directus* pushes on foot, causing upstroke of valves. (D) Valve contraction, which pushes blood into the foot, inflating it to form a terminal anchor. (E) Contraction of the foot, which draws valves downward. (F) Expansion of the valves, at the start of the next burrowing cycle.

Blunt body drag measurement

The device shown in Fig. 2 was used to measure drag force on the valves of *E. directus* static soil. The device was constructed from a pair of *E. directus* valves bonded to an aluminum rod with a urethane casting compound (McMaster-Carr #8690K1, Princeton, NJ, USA). The valves were positioned in their natural orientation and the cross-sectional area of the rod was less than the frontal area of the valves, as to minimize its effect on drag. A fish scale (Jennings Ultrasport 30, www.jscale.com) attached to a pushing handle was mounted to the top of the rod to measure insertion force. The device was operated by slowly pushing it into the soil (as to avoid inertial effects) and recording the force at each depth increment marked on the rod.

Visualization tank

The adage 'clear as mud' is used to describe the difficulty of visually investigating burrowing animals *in situ*. To surmount this challenge and view the burrowing motions of *E. directus*, as well as deformations in the soil surrounding the animal, we developed the visualizer shown in Fig. 3A. The visualizer is essentially a backlit ant farm, or Hele-Shaw cell, which is commonly used in fluid mechanics experiments to measure flow in two dimensions (Kundu and Cohen, 2004). The front viewing pane is adjustable forward and aft via a lead screw and bellowed side walls, allowing tank and animal thickness to be matched. Specimens were oriented vertically in the visualizer with their valves orthogonal to the tank walls (Fig. 3B). This forced a plane strain condition while allowing for soil deformation in the principal directions of the animal's burrowing motions.

The substrate used in the visualizer is composed of 1 mm diameter, optically clear soda-lime glass beads (Potters Industries A-100, Malvern, PA, USA). This substrate was chosen because its particle size and density (ρ=2.52 g cm^{-3}) are close to that of coarse silica sand (Terzaghi et al., 1996), one of the substrates in which razor clams live (Holland and Dean, 1977). Although smaller substrate particles are more common in *E. directus* habitat, we found through experimentation that soda-lime glass beads less than 1 mm in diameter did not provide adequate light transmission for visualization.

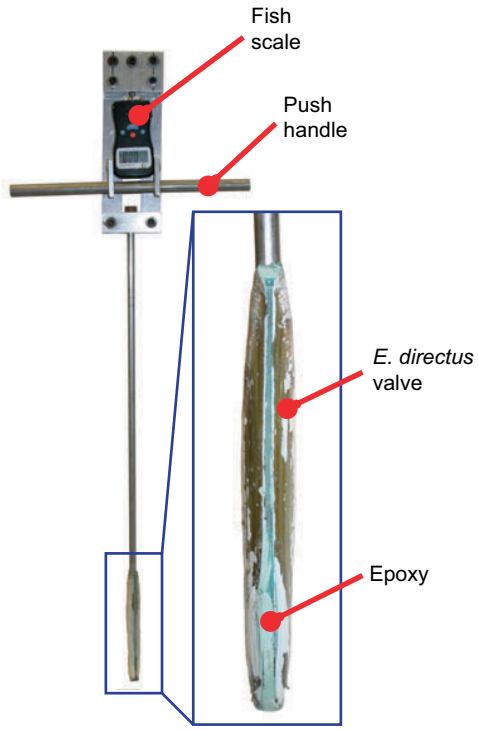

Fig. 2. Blunt body drag measurement device. The end of the device is made from real *E. directus* valves in their natural configuration. Pushing it into soil gives a measure of drag forces experienced by *E. directus* without localized fluidization. Force measurements are read from the fish scale.

Heat dissipation was an important consideration in the visualizer design, as the halogen lamps generate sufficient heat to melt the polycarbonate walls of the tank (and kill the animals) within minutes if not actively cooled. Chilled and oxygenated water supplied from the commercial lobster tank used to hold specimens is circulated through the visualizer (Fig. 3C). This water is mixed with hot water flowing out of the visualizer and gravity fed into a pump. The pump sends water to a reservoir with a float valve that maintains fill level near the top of the visualizer. Two outlets leave the reservoir: one into the top of the visualizer and one directly back to the lobster tank. The flow rate through the visualizer is 10 gallons min^{-1}, which yields a downwards bulk flow velocity of ~0.08 cm s^{-1}. This is 15 times slower than the uplift velocity of *E. directus* (Trueman, 1967) and was therefore assumed to not interfere with burrowing motions.

Because the flow resistance through the substrate within the visualizer is much greater than the resistance of the 'short circuit' line from the reservoir to the lobster tank, the portion of heated water that enters the supply stream at the pump is small compared with the chilled water from the lobster tank. As a result, we were able to maintain temperature in the visualizer to within 2°C of the lobster tank, which was set to 10°C.

Valve kinematics tracking

Ensis directus specimens placed in the visualizer were filmed with a high-definition video camera (Sony HD Handycam, Tokyo, Japan) at 30 frames s^{-1}. During some tests, the animals were stimulated to dig by lightly touching their siphons. In most tests, *E. directus* burrowed naturally without any applied stimulus. Each test was composed of one complete burrowing cycle (Fig. 1). The data presented in this paper represent 23 burrowing cycles performed by three separate animals at a depth ranging from 0.5 to 1 body lengths.

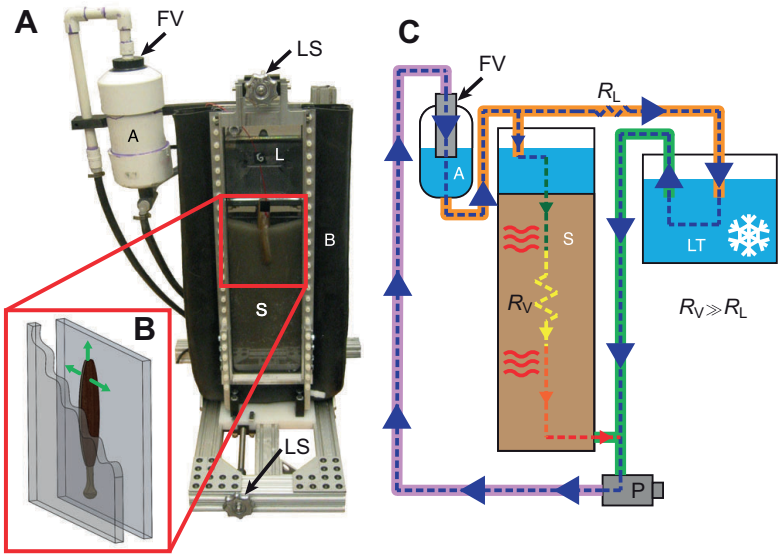

Fig. 3. Burrowing visualization system. (A) Visualization tank filled with 1 mm soda-lime glass beads. Viewing panes are adjustable *via* lead screws to match tank and animal width, forcing a plane strain condition. Labeled regions: FV, float valve; A, accumulator; LS, lead screw; L, 500 W halogen light; B, bellowed sidewall; S, substrate. (B) Schematic of the orientation of *E. directus* within the visualizer. Green arrows denote the principal directions of valve movement. (C) Flow diagram of the visualizer's cooling and recirculation system. Chilled water, fed by gravity from a commercial lobster tank (LT), is mixed with warm water from the visualizer and fed into a pump. Water is pumped into the accumulator, which maintains fill level in the visualizer *via* a float valve. The outlet from the accumulator feeds both the visualizer and a 'short circuit' line back to the lobster tank. As the resistance through the visualizer, R_V, is much greater than the short circuit line resistance, R_L, nearly all of the water flowing from the pump and into the visualizer is fresh from the lobster tank.

Kinematics of *E. directus* were tracked using the following process: (1) frames of each digging cycle were converted to 720×480 pixel grayscale images (Fig. 4A); (2) each image was converted to black and white in MATLAB (The MathWorks, Natick, MA, USA), with a threshold chosen to accentuate the contrast between dark areas of the valves and light areas of the foot and substrate; (3) the images were filtered to remove all connected components consisting of fewer than 50 pixels, which removed dark areas that do not correspond to the valves; and (4) the remaining points were divided into four quadrants that approximate the top, bottom, left and right sides of the valves using a rectangular orthogonal regression algorithm (Arbenz, 2008). The size and position of this rectangle was then used to identify the width and depth of the clam in each video frame of each test (Fig. 4A).

Particle image velocimetry analysis

To measure substrate deformations around burrowing *E. directus*, opaque particles were interspersed in the visualizer substrate at a concentration of 7% and were tracked using MatPIV particle image velocimetry (PIV) software (Sveen, 2004). Raw video from each of the 23 burrowing cycle tests was converted to grayscale and cropped to show only the substrate to one side of *E. directus* (Fig. 4A). This removed tracking artifacts generated by the motion of the valves and the shadow projected by the animal's body. The substrate to the side of *E. directus* that exhibited the greatest displacement was used for PIV analysis (causes for asymmetry are discussed in the Results). Each video frame was then converted to a 720×480 pixel image. Adjacent images were processed with MatPIV in three iterations with interrogation windows of 64×64, 32×32 and 16×16 pixels, all with 50% overlap.

The mechanical properties of soils largely depend on void fraction, ϕ, which is the fractional amount of the substrate's volume occupied by voids (liquid or gas). PIV data were used to calculate the instantaneous void fraction field around *E. directus* with the following method. The displacement field, $\partial\delta_i$, between subsequent video frames, was calculated using the velocity, v, measured *via* PIV, and time, t, between frames:

$$\partial\delta_i = v_i dt = \frac{\partial\delta_i}{\partial t} dt \ . \qquad (1)$$

Displacements between each video frame were summed to find the total horizontal and vertical displacement fields. At the point of valve contraction (Fig. 1D), immediately before valve penetration (Fig. 1E), the mean (±s.d.) horizontal displacement of the soil adjacent to the animal for all tests was found to be 9.2±4.9 times greater than the vertical displacement. As a result, horizontal soil displacement was considered to be the most important factor in the animal's manipulation of the substrate. To reduce PIV noise, horizontal displacement as a function of horizontal position was determined by averaging the rows of the horizontal displacement field (Fig. 4B).

Volumetric strain (e) in an element of soil was calculated as:

$$e = \frac{V^t - V_0^t}{V_0^t} \ , \qquad (2)$$

where V^t is the current and V_0^t is the initial volume of the element. A volumetric strain field was calculated by summing the principal strain fields, ε_i. As a result of the disparity between measured horizontal and vertical displacements in our PIV data, and because the visualizer imposed a plane strain condition, we approximated the strain field around burrowing *E. directus* as $e \approx \varepsilon_x = \partial\delta_x/\delta x$. A smooth function for δ_x was required to evaluate this derivative without generating excessive noise; for each burrowing test, an exponential function was fit to the horizontal displacement data (Fig. 4B). Only tests with fits of $R^2 > 0.9$ were used in our analysis, which yielded the 23 data sets reported in this work.

To calculate changes in void fraction at a point, the same control volume must be used before and after deformation, in this case the initial volume of the differential element, V_0^t. The initial void fraction is then $\phi_0 = 1 - V_0^s/V_0^t$ and the final void fraction is $\phi = 1 - V^s/V_0^t$, where the amount of solids remaining in V_0^t after deformation, V^s, is equal to $V_0^s(V_0^t/V^t)$. Combining Eqn 2 with the previous relationships yields an expression for the current void fraction, ϕ, given the initial void fraction, ϕ_0, and the volumetric strain:

$$e = \frac{V_0^s - V^s}{V^s} = \frac{\phi - \phi_0}{1 - \phi} \Rightarrow \frac{e + \phi_0}{1 + e} = \phi \ . \qquad (3)$$

With Eqn 3, temporal changes in void fraction around burrowing *E. directus* were calculated from PIV data (Fig. 4B). The only initial condition required was the initial void fraction, which was determined to be 0.38 by measuring the volume of the experimental setup and the volume of the pore fluid.

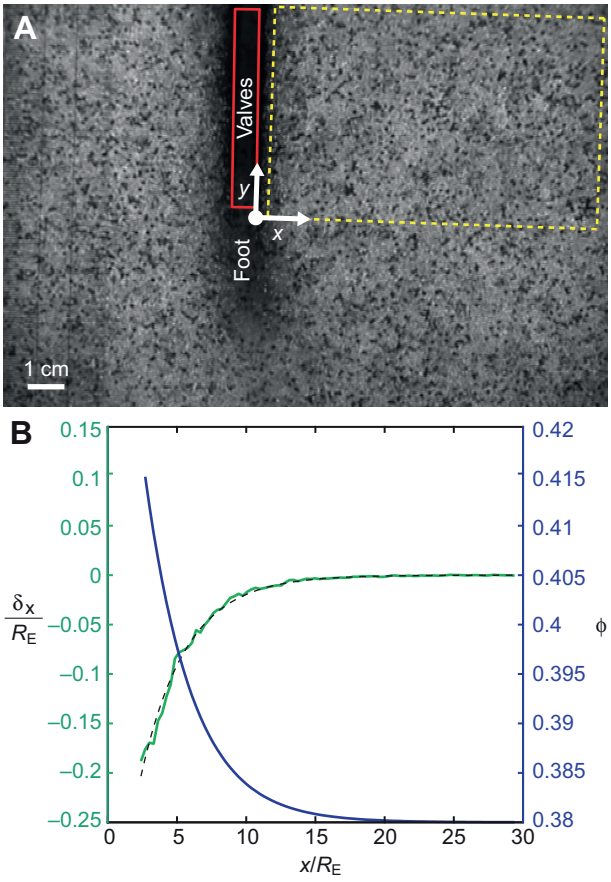

Fig. 4. Clam tracking and soil unpacking from particle image velocimetry (PIV) data. (A) Grayscale image from raw video showing the valves and foot of *E. directus*. The red box denotes the boundary of the valves, determined by tracking software. The yellow box outlines the area of substrate investigated with PIV. Soil and valve displacements were measured in reference to the animal's initial valve position, shown by the white coordinate system. (B) Example of soil displacement and unpacking after valve contraction (Fig. 1D) and before valve penetration (Fig. 1E). Horizontal displacement from PIV data, δ_x (green line), have been averaged over the height of the interrogation window to produce a function that varies only in horizontal position, *x*. The dashed line is an exponential fit to the data. The blue line is the void fraction in the soil, ϕ, calculated from the exponential fit. All lengths have been non-dimensionalized by the initial radius of *E. directus*, R_E.

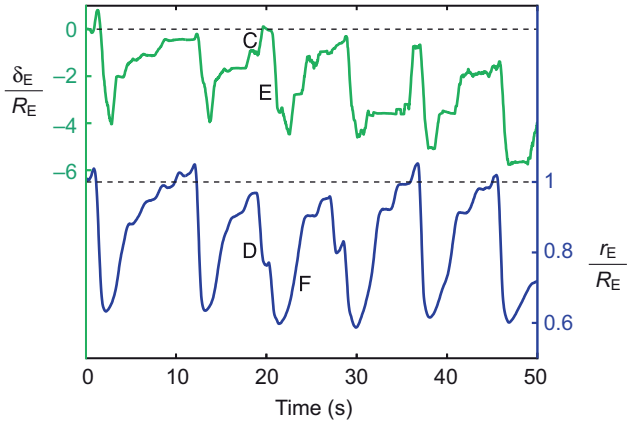

Fig. 5. Measured burrowing kinematics. (A) Vertical and radial valve positions, δ_E and r_E, respectively, of an *E. directus* specimen during five consecutive burrowing cycles. Sections of the burrowing cycle that correspond to Fig. 1C–F are labeled on the third cycle. Dashed lines show initial positions. Lengths have been non-dimensionalized by the initial radius of *E. directus*, R_E.

RESULTS

Fig. 5 shows valve kinematics during five consecutive burrowing cycles for one of the *E. directus* specimens tested. Each stage of the burrowing behavior, corresponding to Fig. 1C–F, can be seen. The digging progress per cycle is small but apparent. Each stage of the digging motion does not happen discretely; contraction (Fig. 1D) continues during penetration (Fig. 1E) and the valves tend to rise during expansion (Fig. 1F).

Fig. 6 shows the temporal changes in substrate displacement during one *E. directus* burrowing cycle. Valve uplift (Fig. 6B) and contraction (Fig. 6C) result in a local soil disturbance. The magnitude of the particle motion on either side of the animal was rarely symmetric. This result is expected if *E. directus* lies at a slight angle relative to vertical; the substrate on the uphill side of the animal will preferentially deform by sliding downwards, rather than the substrate on the downhill side of the animal deforming by sliding upwards (Terzaghi et al., 1996). This behavior is consistent with our observations. Soil deformations caused by the valve motions *E. directus* occurred on a time scale smaller than that required for the soil to collapse and fill around the animal. The natural failure wedge that occurs in this condition can be seen in Fig. 6D, with the matching overlaid failure angle, θ_f, which was calculated from the soil's friction angle. The relationship between friction and failure angle is explained in the Discussion.

Void fraction values calculated from PIV displacement data taken at the point of valve contraction (Fig. 1D) that immediately precedes valve penetration (Fig. 1E) show that these burrowing motions unpack and locally fluidize the substrate proximate to *E. directus* (Fig. 7). The void fraction at incipient fluidization for the substrate was assumed to be ≈0.41, which is consistent with the level measured by Wen and Yu for substrate particles of similar size, shape and density (Wen and Yu, 1966). Table 1 reports the horizontal displacement functions that were fit to the horizontal displacement PIV data to calculate changes in void fraction and the location of the fluidized zone. These functions were used to extrapolate data (gray dotted lines in Fig. 7) for the shadow regions between the animal's body and the cropped video frames (Fig. 4A).

DISCUSSION

Fluidization due to *E. directus* valve contraction

As *E. directus* contracts its valves, it reduces the level of stress acting between the valves and the surrounding soil. At some stress level, the imbalance between horizontal and vertical stress causes the soil adjacent to the animal to fail. Continued valve contraction draws pore water towards the animal, which mixes with the failed soil to create a region of localized fluidization.

The stress state in soil at equilibrium and failure can be represented as Mohr's circles (Hibbeler, 2000) on a normal *versus* shear stress plot (Fig. 8). Failure occurs when the internal shear stress equals the shear strength. Graphically, this is represented when circle b in Fig. 8 is tangent to the failure envelope formed by the soil's friction angle, φ. The stress state shown in Fig. 8 relates to a cohesionless soil; for a cohesive soil, the same failure analysis can be used, but the failure envelope will be shifted vertically by half the soil's cohesive strength.

When *E. directus* first starts to contract its valves, it brings the soil to a state of active failure (Terzaghi et al., 1996). At this point the soil will tend to naturally landslide downward at a failure angle,

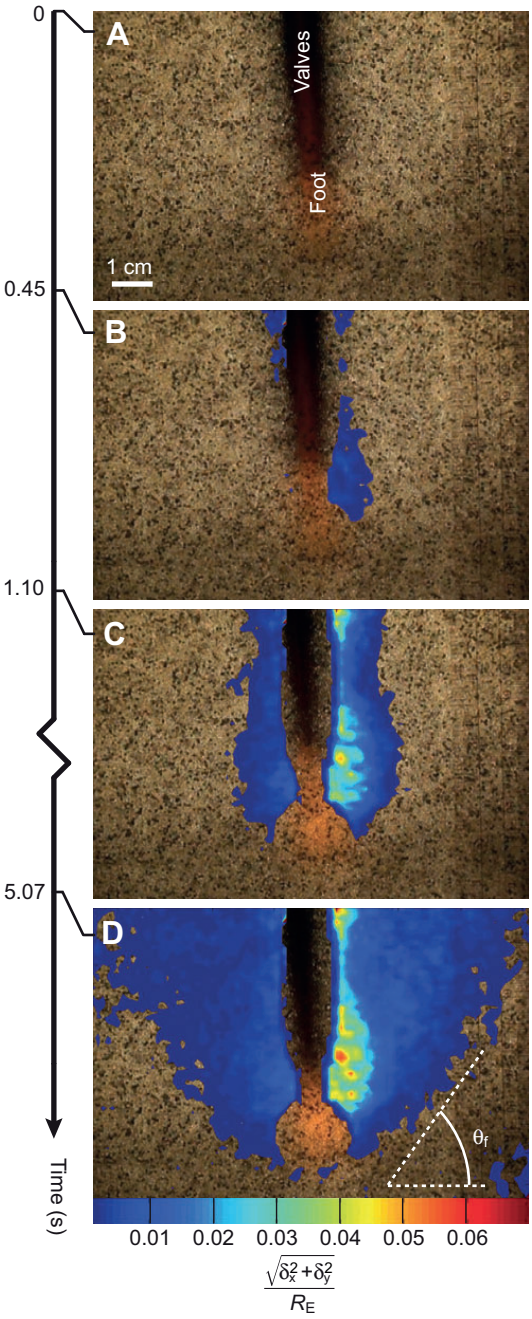

Fig. 6. Soil movement around burrowing *E. directus*. Horizontal and vertical displacement fields from PIV data, δ_x and δ_y, respectively, are plotted together as displacement magnitude, non-dimensionalized by the initial radius of *E. directus*, R_E. Data are overlaid on original video frames used for PIV. The animal's body is masked from the data. The color bar spans 0.001 to 0.07. The timeline shows the progression of burrowing events: (A) initiation of burrowing cycle; (B) completion of valve uplift (Fig. 1C); (C) valve contraction (Fig. 1D), immediately before valve penetration (Fig. 1E); and (D) moment when failure wedge fully forms, occurring after retraction of foot and downwards pull on valves (to Fig. 1E). The predicted failure wedge angle, θ_f, is calculated from the substrate friction angle and is shown with a white dashed line.

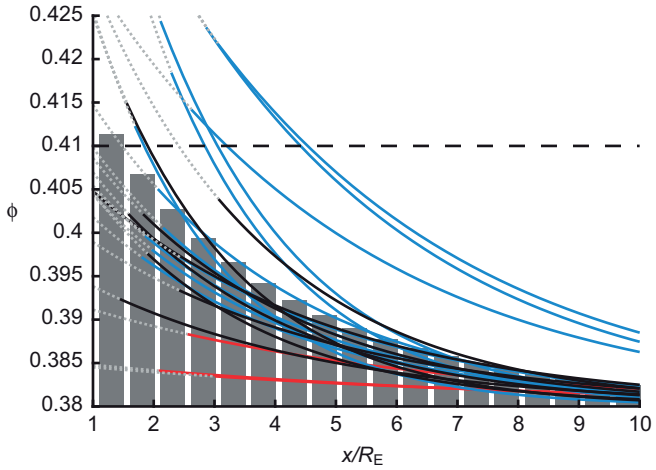

Fig. 7. Localized fluidization around burrowing *E. directus*. Each curve corresponds to void fraction in the substrate, ϕ, as a function of horizontal position, *x*, for 23 burrowing tests taken at the point of valve contraction (Fig. 1D), immediately before valve penetration (Fig. 1E). Position has been non-dimensionalized by the initial radius of *E. directus*, R_E. Solid lines were calculated from PIV horizontal displacement data (red, animal a; black, animal b; blue, animal c). Gray dotted lines are extrapolations through the shadow zone between the animal's valves and the section of soil investigated with PIV (Fig. 4A). Gray bars are the average void fraction for all tests (including extrapolated data) in characteristic lengths away from the animal. The black dashed line is the incipient fluidization void fraction. These data show that soil proximate to *E. directus* becomes fluidized during valve uplift and contraction.

θ_f, illustrated by inset b in Fig. 8. The failure angle is the transformation angle between the principal stress state and the stress state at the tangency point between the circle and failure envelope. This angle can also be seen in Fig. 8 by connecting the tangency point on the failure envelope, the horizontal failure effective stress, σ'_{hf}, and the principal stress axis, and is given by $\theta_f=(\pi/4)+(\varphi/2)$. Effective stresses, indicted with a prime, represent the actual stress between soil particles, neglecting hydrostatic pressure of the pore fluid.

We observed that valve uplift and contraction occur on a smaller time scale than that required to form a landslide failure wedge in the substrate around burrowing *E. directus* (Fig. 6B–D). This gives the animal time to move through the fluidized soil before it collapses. The calculated failure angle in the visualizer substrate, determined *via* the friction angle (measured as 25 deg for 1 mm soda-lime glass beads), aligns with the failure wedge angle observed in the PIV data (Fig. 6D).

Although bulk landslide movement of the soil does not occur when *E. directus* initiates valve contraction, the resulting imbalance in stresses brings the soil to a state of failure, creating a failure surface at angle θ_f. The existence of this failure surface is crucial because it creates a discontinuity in the substrate surrounding *E. directus*, where the soil particles within are free to move and the soil particles beyond remain stationary. As *E. directus* contracts its valves, it reduces its own body volume; this change in volume must be compensated by pore fluid drawn into the failure zone. Increasing the pore fluid while retaining the same number of particles within the failure surface results in a net increase in void fraction, creating a fluidized zone around *E. directus*.

The importance of a soil failure surface around contracting *E. directus* is demonstrated by investigating whether motion of pore fluid flow alone could create fluidization. The Reynolds number of the pore fluid adjacent to the valves of *E. directus*, calculated from valve velocity, particle diameter and the pore fluid density and viscosity, varies between 0.02 and 56, depending on particle size [0.002–2 mm (Holland and Dean, 1977; Terzaghi et al., 1996;

Table 1. Horizontal soil displacement fit functions and location of fluidized zone

Animal	Test no.	*A*	*B*	R^2	$\left.\frac{x}{R_E}\right\|_{\phi=0.41}$
a	1	–1.44	–0.0041	0.96	n/a
	2	–1.73	–0.0041	0.96	n/a
	3	–2.72	–0.0053	0.97	n/a
b	1	–5.83	–0.0118	0.99	1.90
	2	–4.80	–0.0086	0.99	n/a
	3	–4.72	–0.0046	0.92	n/a
	4	–3.77	–0.0063	0.98	n/a
	5	–7.80	–0.0055	0.90	2.41*
	6	–7.82	–0.0060	0.99	n/a
	7	–5.12	–0.0061	0.99	n/a
	8	–7.17	–0.0055	0.98	n/a
c	1	–5.25	–0.0121	0.98	1.84
	2	–8.45	–0.0103	0.98	3.04
	3	–7.25	–0.0103	0.98	2.84
	4	–11.92	–0.0066	0.92	4.53
	5	–13.43	–0.0061	0.94	4.41
	6	–10.72	–0.0058	0.95	3.20
	7	–5.96	–0.0051	0.99	n/a
	8	–4.95	–0.0062	0.98	n/a
	9	–6.64	–0.0053	0.99	n/a
	10	–6.22	–0.0059	0.99	n/a
	11	–7.95	–0.0057	0.98	1.48*
	12	–6.21	–0.0051	0.99	n/a

A and *B* correspond to the fitting function $\delta_x=Ae^{Bx}$.
R^2 values are between fit and PIV data.
Fluidization radii marked as n/a have $\phi<0.41$ at $x/R_E=1$. Asterisks indicate extrapolated data at the fluidization point.

Trueman, 1967)], animal size (10–20 cm; A.G.W., personal observations) and valve contraction velocity [$\approx$0.011–0.028 m s^{-1} (Trueman, 1967)]. As this range mostly falls within the regime of Stokes drag (Kundu and Cohen, 2004), the characteristic time for a particle to reach valve velocity during contraction can be estimated by conservation of momentum, given by:

$$m_p\frac{dv_p}{dt}=6\pi\mu_f d_p\left(v_v-v_p\right)\Rightarrow t_{char}=\frac{d_p^2\rho_p}{36\mu_f}\ , \tag{4}$$

where m_p is the mass of the particle, μ_f is the pore fluid viscosity, v_v is the valve contraction velocity, v_p is the particle velocity, t_{char} is the time constant of the differential equation governing velocity change and ρ_p is the density of the particle.

This analysis yields time scales of 0.075 s for 1 mm soda-lime glass beads in water. These time scales are considerably less than the ~0.2 s valve contraction time measured by Trueman (Trueman, 1967) and the contraction time of 1.46±0.58 s (mean ± s.d.) measured in our tests. Furthermore, 1 mm particles represent an upper bound for *E. directus* habitat; the time scale mismatch is even greater for smaller substrate particles. As such, soil particles surrounding *E. directus* can be considered inertia-less and are advected with the pore fluid during valve contraction.

The presence of a failure surface breaks the coupling between particles and pore fluid movement; particles within the failure wedge can freely move and fluidize, whereas particles outside remain static. Without the wedge, an initially uniform particle distribution would remain uniform as substrate particles follow the pore fluid flow, which is incompressible and governed by $\nabla\cdot\mathbf{v}=0$. No divergence in the flow field implies no divergence between particles, and thus no unpacking.

Fluidization due to *E. directus* uplift motion

A fluidized bed is created when fluid flows upwards (against gravity) through a substrate and the resulting pressure gradient, neglecting hydrostatic pressure, supports the weight of the particles. A common example of a fluidized bed is quicksand, where fluid pressure beneath the soil surface is great enough to induce upwards flow and levitate the soil. The bulk fluid flow velocity (as opposed to the flow velocity within the void spaces between particles) to induce fluidization is the same as the settling velocity of a fluidized bed at incipient fluidization. Wen and Yu derived two expressions for the void fraction at incipient fluidization, ϕ', from tests of different size, density and shape particles (Wen and Yu, 1966):

$$\frac{1-\phi'}{\psi^2\left(\phi'\right)^3}\cong 11,\frac{1}{\psi\left(\phi'\right)^2}\cong 14\ , \tag{5}$$

where ψ is the particle shape factor ($\psi\approx1$ used for round particles).

Using a series of empirically derived correlations, we can relate ϕ' to the velocities required for fluidization. Richardson and Zaki (Richardson and Zaki, 1954) reported that the relationship between settling velocity of particles in fluid, v_s, and a single particle's terminal velocity in an infinite fluid, v_t, depends on the void fraction raised to the power *n*:

$$v_s=v_t\phi^n\ . \tag{6}$$

To find *n*, we use the correlation determined by Khan and Richardson (Khan and Richardson, 1989), which relates the void fraction exponent and Archimedes number, Ar, a dimensionless number that corresponds to the motion of fluids due to differences in density:

$$\frac{4.8-n}{n-2.4}=0.043\mathrm{Ar}^{0.57},\ \mathrm{Ar}=\frac{gd_p^3\rho_f\left(\rho_p-\rho_f\right)}{\mu_f^2}\ , \tag{7}$$

where $\boldsymbol{g}$ is the gravitational constant, d_p is the particle diameter, ρ_f is the density of the fluid, ρ_p is the density of the particle and μ_f is

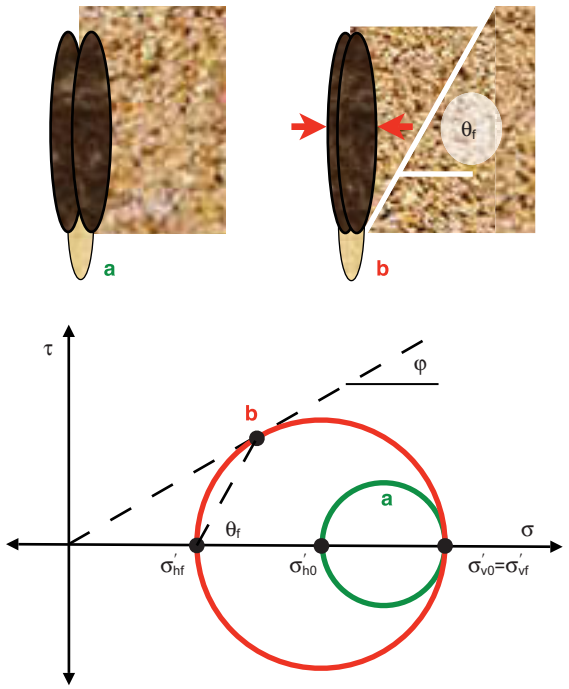

Fig. 8. Induced soil failure by valve contraction, showing Mohr's circle of equilibrium (a) and active failure (b) stress states. Inset b shows the formation of a failure surface at angle θ_f and the tendency of soil to naturally landslide during valve contraction, indicated by red arrows. φ, friction angle; τ, shear stress; σ, normal stress; σ'_{h0} and σ'_{v0}, horizontal and vertical effective stress, respectively, at equilibrium; σ'_{hf} and σ'_{vf}, horizontal and vertical effective stress, respectively, at failure.

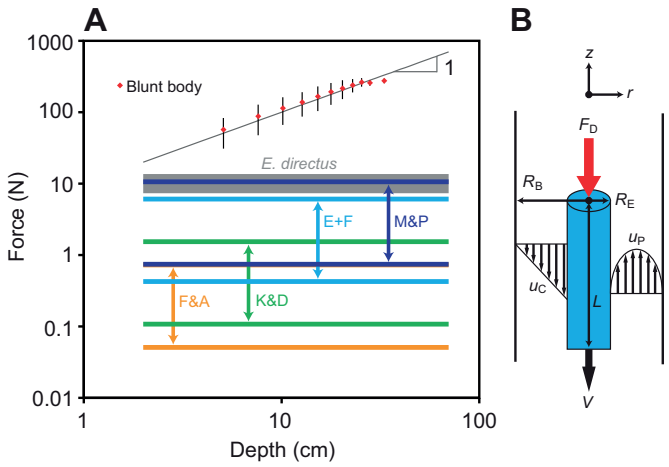

Fig. 9. Drag forces on burrowing *E. directus*. (A) Drag force as a function of depth for static and fluidized soil. The gray bar is the maximum pulling force of *E. directus* measured by Trueman (Trueman, 1967). Data points are from penetration tests in *E. directus* habitat using the blunt body shown in Fig. 2 (error bars indicate ±s.d.; N=13). Drag force ranges in fluidized substrate calculated using $1<R_B/R_E<3$ and the following liquid/particle viscosity models: F&A (Frankel and Acrivos, 1967); K&D (Krieger and Dougherty, 1959); E+F (Eilers, 1941; Ferrini et al., 1979); and M&P (Maron and Pierce, 1956). The plot shows that although *E. directus* is not strong enough to move through a static substrate, drag forces experienced in fluidized substrates are within its strength capabilities. (B) Model of liquid/particle flow around *E. directus* used to predict fluid drag. Total flow around animal is sum of Couette (u_C) and Poiseuille (u_P) flow fields. F_D, pulling force, which is equal to drag force; R_B, burrow radius; R_E, *E. directus* radius; L, *E. directus* length; V, *E. directus* velocity.

the fluid viscosity. The particle terminal velocity can be expressed as $v_t=(\mathrm{Re}_{p,t}\mu_f)/(\rho_f d_p)$, where $\mathrm{Re}_{p,t}$ is the Reynolds number for the particle at terminal velocity. Finally, the Reynolds number can, in turn, be calculated regardless of whether the flow is dominated by viscous or inertial effects using a correlation to the Archimedes number, developed by Gibilaro (Gibilaro, 2001):

$$\mathrm{Re}_{p,t} = [-3.809 + (3.809^2 + 1.832\mathrm{Ar}^{0.5})^{0.5}]^2 . \quad (8)$$

Combining Eqns 5–8 enables us to compute the settling velocity, and thus the required bulk upward fluid flow velocity, at the incipient fluidization void fraction. The fluidization velocity at $\phi'=0.41$ for 1 mm soda-lime glass beads is 1.35 cm s^{-1}. The uplift velocity of *E. directus* measured by Trueman is 1.25 cm s^{-1} (Trueman, 1967). The peak uplift velocity during the uplift stroke (shown by segment C on Fig. 5A) measured in our experiments where there was a clearly distinguishable upward jerk before valve penetration was 1.30±0.89 cm s^{-1} (mean ± s.d., N=18). This means that the uplift motion of *E. directus* induces a velocity in the pore fluid on the order of the velocity required to fluidize the substrate below the animal. Furthermore, 1 mm is near the upper bound of particle size in *E. directus* habitat; using the same uplift velocity, *E. directus* can easily fluidize smaller particles. For example, spherical 0.5 mm soda-lime glass beads will reach $\phi'=0.41$ at an upward flow velocity of 0.5 cm s^{-1}.

Burrowing drag reduction due to localized fluidization

Moving through fluidized, rather than static, soil provides considerably less drag resistance for *E. directus*, as stresses – normally concentrated in force chains (Cates et al., 1998) – cannot be transferred between particles. The model shown in Fig. 9B depicts the flow fields and drag force experienced by *E. directus* while moving through a fluidized substrate. We chose to use a three-dimensional (3-D) model for this analysis, rather than a two-dimensional model based on our visualizer, because: (1) *E. directus* lives in three dimensions; (2) the blunt body data in Fig. 9A were gathered in real, 3-D ocean substrate; and (3) the size of the fluidized zone shown in Fig. 7 is consistent with other 3-D measurements and calculations (Winter, 2011). The flow field around burrowing *E. directus* is composed of summed Couette (u_C) and Poiseuille (u_P) flows (Kundu and Cohen, 2004) in an annulus (Fig. 9B), with:

$$u_C = -V\frac{\ln\left(\frac{r}{R_B}\right)}{\ln\left(\frac{R_E}{R_B}\right)} , \quad (9)$$

and

$$u_P = \frac{1}{4\mu_{eff}}\left(\frac{-dp}{dz}\right)\left[R_B^2 - r^2 + \frac{R_B^2 - R_E^2}{\ln\left(\frac{R_E}{R_B}\right)}\ln\left(\frac{R_B}{r}\right)\right] , \quad (10)$$

where V is the penetration velocity of *E. directus*, R_E is the animal's radius, R_B is the burrow radius, r is the radial coordinate from the center of animal, μ_{eff} is the effective viscosity of the liquid and particle mixture, p is the pressure driving the Poiseuille flow and z is the axial coordinate. From conservation of mass, the volume per unit time displaced by *E. directus* must equal the volumetric flow

Table 2. Effective viscosity models depending on void fraction, ϕ

	Expression	Reference
μ_{eff} =	$\mu_f\left(\frac{9}{8}\right)\frac{\left(\frac{1-\phi}{1-\phi'}\right)^{\frac{1}{3}}}{1-\left(\frac{1-\phi}{1-\phi'}\right)^{\frac{1}{3}}}$	Frankel and Acrivos, 1967
	$\mu_f\left(1-\frac{1-\phi}{1-\phi'}\right)^{-2.5\phi'}$	Krieger and Dougherty, 1959
	$\mu_f\left[1+\frac{1.25(1-\phi)}{1-\frac{1-\phi}{1-\phi'}}\right]^2$	Eilers, 1941; Ferrini et al., 1979
	$\mu_f\left(1-\frac{1-\phi}{1-\phi'}\right)^{-2}$	Maron and Pierce, 1956

μ_{eff}, effective viscosity of the liquid and particle mixture; μ_f, pore fluid viscosity.

rate of liquid/particle mixture pushed upwards past the animal's body:

$$\pi V R_E^2 = \int_{R_E}^{R_B}\left(u_C + u_P\right)2\pi r\,\mathrm{d}r\ . \quad (11)$$

Evaluating this integral yields an expression for the pressure differential driving the Poiseuille flow. Once this differential is known, the total force acting on *E. directus*, F_D, can be found by summing the forces caused by the pressure differential and skin friction:

$$F_D = \pi R_E^2\frac{-\mathrm{d}p}{\mathrm{d}z}L + 2\pi R_E L\mu_{eff}\frac{\mathrm{d}}{\mathrm{d}r}\left[u_C + u_P\right]_{R_E}\ . \quad (12)$$

To evaluate Eqn 12, the effective viscosity of the liquid and particle mixture, μ_{eff}, must be determined. Fig. 9A juxtaposes the pulling capabilities of *E. directus* in static substrates, determined through tests with the blunt body in Fig. 2, and drag forces calculated with Eqn 12 using the effective viscosity models in Table 2, which depend on void fraction at incipient fluidization.

As the void fraction at incipient fluidization in *E. directus* habitat was not known, we estimated ϕ' to be 0.399, which is the average of the expressions in Eqn 5 with round particles. Variation in burrow radius corresponds to the zone in Fig. 7 where the mean plus one standard deviation in void fraction is above the incipient fluidization threshold ($1<r/R_E<3$). The fluidized void fraction was taken to be the largest mean value in Fig. 7, $\phi'=0.411$. The radius used for the animal was $R_E=1.6$ cm. Maximum downwards velocity (10 cm s^{-1}) and pulling force of the animal (10 N) were measured by Trueman (Trueman, 1967). Although *E. directus* is too weak to move through static soil, the data shown in Fig. 9A demonstrate that moving through fluidized soil lowers drag forces to within the animal's strength capability.

Energetic savings from burrowing through fluidized substrate

Data adapted from Trueman's measurements of burrowing *E. directus* (Trueman, 1967) compared with the blunt body energetics calculated from force data shown in Fig. 9A show that moving through fluidized, rather than static, soil reduces the amount of energy *E. directus* has to expend to reach full burrow depth by an order of magnitude (Fig. 10). In an idealized fluidized medium, the drag force on a body does not depend on depth. Moving through a packed, static particulate medium, as in the case of the blunt body, requires pushing force that increases linearly with depth (Robertson and Campanella, 1983). As a result, burrowing energy, calculated by $E=\int F\mathrm{d}z$, scales linearly with depth for *E. directus*, rather than with depth squared for the blunt body.

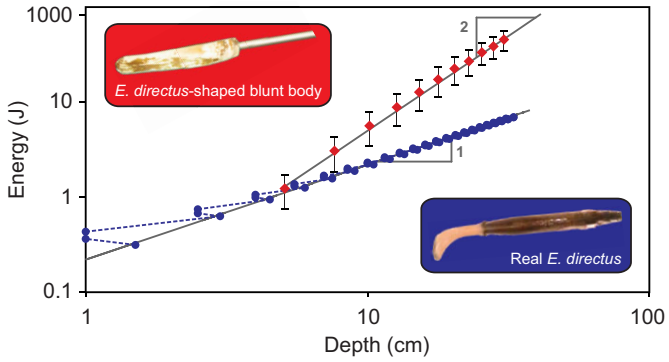

Fig. 10. Energetic savings achieved *via* localized fluidization burrowing. The blunt body shown in Fig. 2 requires an order of magnitude more energy to reach full burrow depth than real *E. directus* (error bars indicate ±s.d.; N=13). Using localized fluidization, burrowing energy scales linearly with depth, rather than with depth squared for moving through static substrate.

ACKNOWLEDGEMENTS

The authors thank C. Becker, M. Bollini, D. Dorsch, J. Kao, K. Ray and D. Sargent for their experimental and analytical assistance.

FUNDING

This work was funded by the Battelle Memorial Institute, Bluefin Robotics and the Chevron Corporation.

REFERENCES

Arbenz, P. (2008). Fitting a rectangle. Einführung in MATLAB. Zurich: Department of Computer Science, ETH Zürich. Available at: http://www.inf.ethz.ch/personal/arbenz/MatlabKurs/node88.html.

Cates, M. E., Wittmer, J. P., Bouchard, J. P. and Claudin, P. (1998). Jamming, force chains, and fragile matter. *Phys. Rev. Lett.* **81**, 1841-1844.

Dorgan, K. M., Jumars, P. A., Johnson, B., Boudreau, B. and Landis, E. (2005). Burrowing mechanics: burrow extension by crack propagation. *Nature* **433**, 475.

Eilers, H. (1941). The viscosity of the emulsion of high viscosity materials as function of concentration. *Kolloid Z.* **97**, 313-321.

Energizer (2009). Energizer E91 AA battery product datasheet. Available at: http://data.energizer.com/PDFs/E91.pdf.

Fager, E. W. (1964). Marine sediments: effects of a tube-building polychaete. *Science* **143**, 356-358.

Ferrini, F., Ercolani, D., de Cindio, B., Nicodemo, L., Nicolais, L. and Ranaudo, S. (1979). Shear viscosity of settling suspensions. *Rheologica Acta* **18**, 289-296.

Frankel, N. A. and Acrivos, A. (1967). On the viscosity of a concentrated suspension of solid spheres. *Chem. Eng. Sci.* **22**, 847-853.

Gibilaro, L. G. (2001). *Fluidization-Dynamics.* Oxford: Butterworth-Heinemann.

Hibbeler, R. C. (2000). *Mechanics of Materials.* Upper Saddle River, NJ: Prentice Hall.

Holland, A. F. and Dean, J. M. (1977). The biology of the stout razor clam *Tagelus plebeius*: I. Animal–sediment relationships, feeding mechanism, and community biology. *Chesapeake Sci.* **18**, 58-66.

Jung, S. (2010a). *Caenorhabditis elegans* swimming in a saturated particulate system. *Physics Fluids* **22**, 031903.

Jung, S., Winter, A. G., Hosoi, A. E. (2010b). Dynamics of digging in wet soil. *Int. J. Non-Linear Mech.* **46**, 602-606.

Khan, A. R. and Richardson, J. F. (1989). Fluid–particle interactions and flow characteristics of fluidized beds and settling suspensions of spherical particles. *Chem. Eng. Commun.* **78**, 111-130.

Krieger, I. M. and Dougherty, T. J. (1959). A mechanism for non-Newtonian flow in suspensions of rigid spheres. *J. Rheol.* **3**, 137-152.

Kundu, P. K. and Cohen, I. M. (2004). *Fluid Mechanics.* San Diego, CA: Elsevier Academic Press.

Maladen, R. D., Ding, Y., Li, C. and Goldman, D. I. (2009). Undulatory swimming in sand: subsurface locomotion of the sandfish lizard. *Science* **325**, 314-318.

Maron, S. H. and Pierce, P. E. (1956). Application of ree-eyring generalized flow theory to suspensions of spherical particles. *J. Colloid Sci.* **11**, 80-95.

Richardson, J. F. and Zaki, W. N. (1954). Sedimentation and fluidisation: Part I. *Chem. Eng. Res. Design* **75 Suppl.**, S82-S100.
Robertson, P. K. and Campanella, R. G. (1983). Interpretation of cone penetration tests. Part I: Sand. *Can. Geotech. J.* **20**, 718-733.
Shin, P. K. S., Ng, A. W. M. and Cheung, R. Y. H. (2002). Burrowing responses of the short-neck clam *Ruditapes philippinarum* to sediment contaminants. *Mar. Poll. Bull.* **45**, 133-139.
Stanley, S. M. (1969). Bivalve mollusk burrowing aided by discordant shell ornamentation. *Science* **166**, 634-635.
Sveen, J. K. (2004). *An Introduction to MatPIV v. 1.6.1*. Oslo: Department of Mathematics, University of Oslo.
Terzaghi, K., Peck, R. B. and Mesri, G. (1996). *Soil Mechanics in Engineering Practice*. London: Wiley-Interscience.
Trueman, E. R. (1966a). Bivalve mollusks: fluid dynamics of burrowing. *Science* **152**, 523-525.
Trueman, E. R. (1966b). Observations on the burrowing of *Arenicola marina* (L.). *J. Exp. Biol.* **44**, 93-118.
Trueman, E. R. (1967). The dynamics of burrowing in *Ensis* (Bivalvia). *Proc. R. Soc. Lond. B* **166**, 459.
Trueman, E. R. (1975). *The Locomotion of Soft-Bodied Animals*. New York: Elsevier Science & Technology.
Wallace, H. R. (1968). The dynamics of nematode movement. *Annu. Rev. Phytopathol.* **6**, 91-114.
Wen, C. Y. and Yu, Y. H. (1966). Mechanics of fluidization. *Chem. Eng. Progr. Symp. Ser.* **62**, 100-111.
Winter, A. G. (2011). Biologically inspired mechanisms for burrowing in undersea substrates. PhD thesis, Massachusetts Institute of Technology, Cambridge, MA.